Acta Materialia 178 (2019) 228–240

Contents lists available at ScienceDirect

Acta Materialia

journal homepage: www.elsevier.com/locate/actamat

Full length article

Microstructure and microchemistry study of irradiation-induced precipitates in proton irradiated ZrNb alloys

Zefeng Yu [a, *], Chenyu Zhang [a], Paul M. Voyles [a], Lingfeng He [b], Xiang Liu [b], Kelly Nygren [c], Adrien Couet [a, d]

[a] Department of Materials Science and Engineering, University of Wisconsin - Madison, 1509 University Ave, Madison, WI, 53705, USA
[b] Advanced Characterization Department, Idaho National Laboratory, P.O. Box 1625, MS 6188, Idaho Falls, ID, 83415, USA
[c] Cornell High Energy Synchrotron Source, Cornell University, 161 Synchrotron Drive, Ithaca, NY, USA
[d] Department of Engineering Physics, University of Wisconsin - Madison, 1500 Engineering Drive, Madison, WI, USA

ARTICLE INFO

Article history:
Received 8 April 2019
Received in revised form
27 July 2019
Accepted 7 August 2019
Available online 13 August 2019

Keywords:
Irradiation
Microstructure
ZrNb

ABSTRACT

Proton irradiation induced Nb redistribution in Zr-xNb alloys (x = 0.4, 0.5, 1.0 wt%) has been investigated using scanning transmission electron microscopy/energy dispersive X-ray spectroscopy (STEM/EDS). Zr-xNb alloys are mainly composed of Zr matrix, native Zr–Nb–Fe phases, and β-Nb precipitates. After 2 MeV proton irradiation at 350 °C, a decrease of Nb content in native precipitates, as well as irradiation-induced precipitation of Nb-rich platelets (135 ± 69 nm long and 27 ± 12 nm wide) were found. Nb-rich platelets and Zr matrix form the Burgers orientation relationship, $[1\bar{1}1]//[2\bar{1}\bar{1}0]$ and (011)//(0002). The platelets were found to be mostly coherent with the matrix with a few dislocations near the ends of the precipitate. The coherent strain field has been measured in the matrix and platelets by the 4D-STEM technique. The growth of Nb-rich platelets is mainly driven by coherency and dislocation-induced strain fields. Irradiation may both enhance the diffusion and induce segregation of interstitial Nb to the ends of the irradiation induced platelets, further facilitating their growth.

1. Introduction

Zirconium–Niobium (Zr–Nb) alloys have been commonly used as reactor core materials in commercial pressurized water reactors (PWRs) for decades, due to their low neutron absorption, excellent mechanical properties, and lower in-reactor corrosion kinetics and hydrogen pickup compared to Zircaloys. The reasons for better in-pile corrosion and hydriding resistance of Zr–Nb alloys are still unclear, and can be the results of irradiation effects in the Zr–Nb base metal, the Zr oxide or the environment (water) or a coupling of all of the above [1]. Using a so-called "separate effects" experimental approach, many studies have focused on the microstructural and microchemical characterizations of irradiated Zr–Nb base metal to better understanding in-reactor corrosion mechanisms [2–4]. One of the most important microstructural findings in irradiated Zr–Nb base metal is that irradiation induces precipitation of platelets, which would reduce the Nb content in the Zr solid solution. It has been recently shown by atom probe tomography (APT) in Refs. [5,6] that Nb concentration in solid solution indeed decreases upon 2 MeV proton irradiation at 350 °C for doses up to 1 dpa. Despite these significant findings, the growth mechanism of platelets under irradiation is still unclear and there is a lack of conclusive experimental results to highlight the impact of precipitate growth on the redistribution of Nb content in Zr matrix.

In-reactor neutron irradiation studies on both M5® (Zr-1.0Nb) and Zr-2.5Nb alloys show that, in addition to the native precipitates, Nb-rich platelets (up to 60 at.% Nb) described as "needle-like" or "sword-shaped" precipitates within the Zr matrix [2,7]. These elongated nano-precipitates were not found in heat treated non-irradiated samples under the same irradiation time period and temperature, suggesting that these precipitates are irradiation induced, rather than thermally-induced. Proton irradiation (3.6 MeV H^+ at 447 °C up to 0.94 dpa and 2 MeV H^+ at 350 °C up to 1.0 dpa) was also found to induce nucleation of platelets in Zr-2.5Nb and M5® (Zr-1.0Nb) [4,5,8]. Recently, aside from the platelets found in the Zr matrix, APT studies on heavy ion irradiated (4 MeV Ni^{3+}) [9], proton irradiated (2 MeV H^+) [5,6] and neutron irradiated [6] samples have also found Nb-rich and Nb–Fe-rich nanoclusters in the matrix, but with much higher densities than the platelets. The

* Corresponding author.
E-mail address: zyu226@wisc.edu (Z. Yu).

https://doi.org/10.1016/j.actamat.2019.08.012
1359-6454/

continuous reduction of Nb in solid solution due to the precipitation of Nb-rich platelets/clusters is hypothesized to be the cause for the absence of in-reactor corrosion acceleration in Zr–Nb alloys up to 80 GWd/MTU [5,10]. To support this hypothesis, the recently developed coupled-current-charge-compensation (C4) model has predicted that lower Nb content, with the right oxidation states and concentrations in the oxide, would lower the corrosion kinetics of Zr–Nb alloys [11].

Only a few studies have discussed the growth mechanism of irradiation-induced platelets in details. In a study by Coleman et al. [2], the growth of platelets upon neutron irradiation at 570–770 K and 0.6–0.8 dpa was attributed to irradiation enhanced diffusion of Nb. Even though nucleation of platelets appears to be only possible under irradiation, precipitates can still grow larger upon post-irradiation heat treatment. Prior to irradiation, large variations of Nb content, 0.07–0.6 at.%, has been reported in the Zr matrix [5,6,9,12,13]. Thus, the true solubility limit of Nb in Zr–Nb alloys is uncertain, making it difficult to determine if pre-irradiated alloys have reached thermodynamic equilibrium conditions. For neutron irradiated M5® in Ref. [7], the shape of platelets attributed to resulted from minimization of the stress field due to matrix/precipitate interface misfit, or due to anisotropic diffusion of irradiation-induced point defects. The precipitate/matrix interface was coherent along the body of the platelet, whereas the two ends of the precipitate had an incoherent interface [14]. From another perspective, albeit in a different material system, Ni-based alloys containing fine coherent $Ni_3(Al, Ti)$ precipitates have shown that the large area of coherent matrix/precipitate interfaces enhance the recombination of point defects, which would theoretically limits the growth of the precipitates upon irradiation [15]. Lastly, a theoretical calculation of a radiation-modified Zr–Nb phase diagram by Turkin et al. [16] has predicted that under reactor conditions, the platelets coherent with the matrix in the plane of the plate should be stable. Whereas incoherent β-Nb precipitates are unstable because their stability field is located at a temperature higher than under reactor conditions. Despite these few attempts to explain precipitates growth under irradiation, a significant knowledge gap remains for the growth mechanism of irradiation-induced precipitation in Zr–Nb alloys. Understanding the detailed microstructure and microchemistry of the irradiation-induced platelets will be vital to explain their growth and subsequent impact on in-pile corrosion kinetics.

In general, hypothesis of growth mechanism of platelets can be divided under two different pre-irradiation conditions. If the pre-irradiated alloy is not under thermodynamic equilibrium condition, such that the matrix is oversaturated with Nb atoms, the growth should be kinetically limited due to slow Nb diffusion in Zr matrix [6,17]. In this case, growth mechanism of platelets under irradiation should be dominated by irradiation-enhanced diffusion [2,18], which enhances Nb diffusion and accelerates the growth kinetics. Sink strength should not play a significant role in the growth, since it is thermodynamically favorable to nucleate and grow new precipitates for Nb to reach an equilibrium concentration in the matrix. On the other hand, under thermodynamic equilibrium, the Nb content in pre-irradiated Zr matrix should be at the equilibrium concentration predicted by Zr–Nb phase diagram [19]. Then, one of the possible growth mechanisms of irradiation-induced precipitation for an equilibrated solute concentration is irradiation-induced segregation through the inverse Kirkendall effect [18]. In this case, sink strength is important to determine the diffusion of point defects (PDs). Variable bias sinks, such as coherent precipitates, acts as traps for PDs, which are attracted to the coherent precipitates to relieve the strain field produced by misfits between the traps and the matrix [18].

Therefore, to investigate the growth mechanism of irradiation induced precipitates, this paper focuses on scanning transmission electron microscopy/energy dispersive X-ray spectroscopy (STEM/EDS) techniques to measure precipitate composition and density before and after irradiation, to identify phases, to investigate precipitate/matrix orientation relationship, and to construct strain maps in order to provide critical information on the growth mechanism of platelets. This study utilizes binary Zr–Nb model alloys with variations in Nb concentration, proton irradiated up to 1 dpa to generate platelets that are enriched in Nb similar to those observed under in-pile irradiation. Through STEM/EDS and selected area electron diffraction (SAED) analysis, the crystal structure and composition of Nb-rich precipitates are identified and compared. Platelets are mainly imaged by STEM and their density was measured in different alloys. High-resolution (HR)STEM was performed to find the orientation relationship between the precipitates and the matrix. Finally, 4D-STEM, a –state-of-the–art electron microscopy technique, was used as the first attempt to map the strain field around the platelets in Zr matrix. Implications of the results on the growth mechanism of platelets and the impact on the Nb content in the solid solution are then discussed.

2. Experimental procedures

Zr-xNb model alloys (target compositions x = 0.4, 0.5, 1.0 wt %) with a final annealing step at 560–580 °C for 5–10 h as well as the same Zr-0.5Nb with an additional annealing at 1000 °C for 15 min followed by a rapid water quench were studied. The objective of the annealing at 1000 °C was to dissolve all native precipitates and study the effect of irradiation in a Nb supersaturated matrix. The bulk material processing steps can be found in Ref. [20]. The bulk compositions of these Zr-xNb alloys were analyzed through combustion method and the results are shown in Table 1. The actual compositions are relatively close to the target compositions such that we will keep referring to the target compositions to label the alloys. It is worth noting that Fe is the main impurity, with concentration level consistent with industrial alloys [21]. The origin of Fe is likely to be the sponge Zr raw material.

All alloys were irradiated at the University of Wisconsin Ion Beam Laboratory (IBL) using a 2 MeV rastered proton beam to induce a damage level up to 1.0 dpa in the flat region. The flux and dpa rate during irradiation were 3.67×10^{13} ion/cm^{2}s and 2.62×10^{-6} dpa/s, respectively. As recommended in the literature [22], irradiation damage in terms of dpa was calculated based on the simulation using SRIM “Quick” Kinchin-Pease mode. The dpa peak is located about 30 μm below the irradiation surface, while the dpa is relatively flat at 5–20 μm in depth. The samples temperature were closely monitored at 350±5 °C using thermocouples welded on two sacrificial samples and a pre-calibrated IR camera. The details of irradiation setup and bulk sample description can be found in Ref. [5].

The detailed TEM sample fabrication procedures performed at the University of Wisconsin – Nanoscale Imaging and Analysis Center (UW-NIAC) are discussed in supplemental materials (SM) section 1 and shown in Fig. S1. The thickness of each thin film was measured using plasmon peak in electron energy loss spectroscopy [23].

Table 1
Bulk composition measured by combustion method in weight percentage (ppm).

	Nb (ppm)	Fe (ppm)	Al (ppm)	Cr (ppm)	Ni (ppm)	Si (ppm)
Zr-0.4Nb	4690	670	30	50	30	10
Zr-0.5Nb	5270	430	50	30	20	20
Zr-1.0Nb	11270	470	40	40	20	10

300 kV Tecnai-TF30 TEM and 200 kV FEI Titan Aberration-corrected STEM (UW NIAC), 200 KV Titan G2 ChemiSTEM (University of Manchester), and 200 kV Titan Themis 200 ChemiSTEM (Idaho National Laboratory) were used to identify precipitates and to quantify their microchemistry and density. Only the low magnification STEM/EDS images at plane view instead of using specific diffraction vectors are reported in this study. Indeed, the STEM/EDS images at plane views allowed to efficiently locate the irradiation induced platelets, due to their specific elongated shape and the sole presence of Nb and Zr in them, across multiple grains and samples. This was deemed more efficient to increase the statistics for size and density assessments of the particles. The crystal structure files used to simulate diffraction patterns of each phases (α-Zr, β-Nb, Laves phase) in JEMs were downloaded from inorganic crystal structure database (ICSD). High-resolution STEM study on the irradiation induced nano-precipitates using 200 kV FEI Titan STEM equipped with probe corrector were performed at UW-NIAC. High angle annular dark field (HAADF) STEM images were collected with a 24.5-mrad probe semi-convergence angle, 18.9 pA probe current, and HAADF detector range of 5.7–12.6 mrad. The experimental details for 4D-STEM are described in SM section 4.

3. Results

3.1. Unirradiated samples

The native precipitates were characterized and are shown in Fig. 1 for the Zr-xNb model alloys. Bright field STEM images and EDS elemental maps of the Zr-xNb model alloys are presented in Fig. 1 A) recrystallized α-Zr microstructure with similar grain size was confirmed for all alloys. Since the solubility of Nb in these alloys has been confirmed to be less than 0.4 at.% in Ref. [5], the presence of Nb-rich native precipitates is expected and observed. From the convergent beam electron diffraction (CBED) and EDS concentration measurements (see Fig. S2 and Table S1 in SM section 2), native precipitates are observed in the matrix and are identified as b.c.c. β-Nb phase and $Zr(Nb,Fe)_2$ Laves phase [7,24,25]. STEM and CBED analysis are presented in Fig. S2 for the Zr-1.0Nb alloy and are representative of all characterized alloys. The measured diffraction patterns are consistent with diffraction patterns generated by JEMs V3. It should be noted that the $Zr(Nb,Fe)_2$ phase observed is a commonly reported Laves phase. However, due to the large density of native precipitates that contain Fe, only a few of them have been fully characterized using SAED. Therefore, other types of Fe precipitates, such as $(Zr,Nb)_3Fe$ and $(Zr,Nb)_2Fe$, may also exist in the matrix, as reported in Ref. [24]. However, neither Fe itself nor Fe-containing precipitates are the primary focus of this study, so the authors will refer to Laves phases as a general indicator of Zr–Nb–Fe containing precipitates.

Based on the STEM/EDS images, the size distribution of native precipitates in Zr–Nb alloys were measured using ImageJ®. For each sample, particle sizes over at least 5 different grains were measured, representing more than 8000 precipitates in total. Then, the particle sizes were fitted using a probability density function to plot the particle size distribution in Fig. S3. Smaller particle sizes are observed when the bulk Nb concentration decreases from 1 wt% to 0.5 wt%. This shift is expected since Zr-1.0Nb indeed contains larger Nb-rich precipitates after annealing, owes to the Ostwald ripening mechanism. The particle density for each Zr-xNb (x = 0.4, 0.5, 1.0 at.%) is 3.14×10^{19}, 6.04×10^{19} and 1.66×10^{20} precipitates/m^3, respectively. As expected, a higher bulk Nb content leads to higher particle density.

The microstructure resulting from Zr-0.5Nb alloy annealed at 1000 °C, a treatment designed to dissolve all native precipitates prior to irradiation, is presented in Fig. 1 D). Based on the thermodynamic phase diagram, the annealing temperature should cause the h.c.p. α-Zr to transform into b.c.c β-Zr phase. If the subsequent quenching rate is fast enough, β-Zr grains should be retained and all native precipitates should be dissolved in the β-Zr solid solution. However, as reported elsewhere [26] and as observed in Fig. 1 D) β-Zr water quenching actually resulted in the formation of lath martensites in the Zr matrix. The matrix was identified as α-Zr phase from SAED (in Fig. S4) and XRD (in Fig. S5). Some laths are parallel to each other, while others form branch-like patterns. In addition, Nb and Fe are slightly enriched in the laths. Although the objective of obtaining an oversaturated homogeneously distributed Nb solid solution was not achieved, intragranular precipitates were indeed dissolved. Now that the microstructures and microchemistry of unirradiated alloys have been characterized, irradiated alloy characterizations will be presented.

3.2. Irradiated samples

The microstructure and microchemistry of the samples after proton irradiation at 0.55 dpa and 1.0 dpa are shown in Fig. 2. Both irradiated Zr-0.5Nb and Zr-1.0Nb contains elongated precipitates

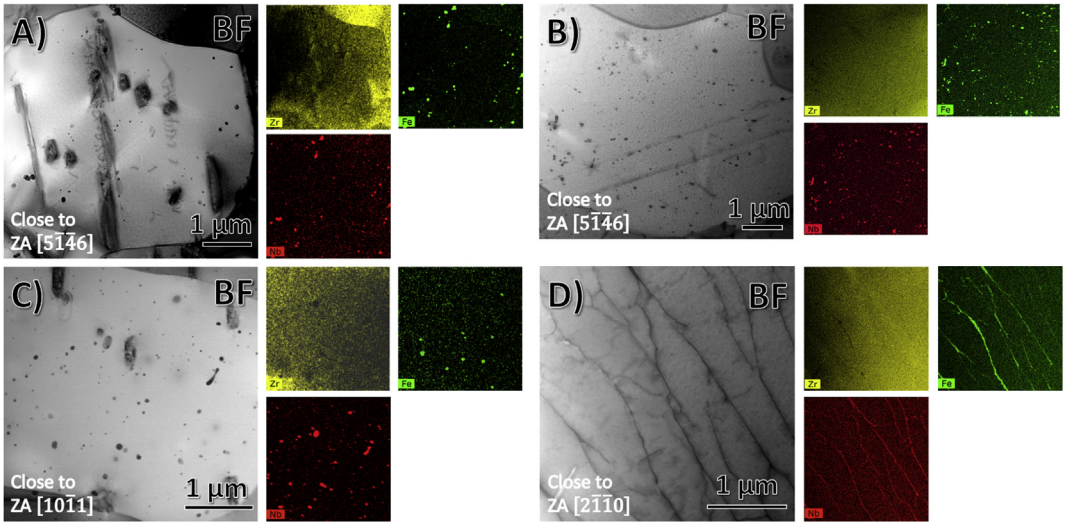

Fig. 1. BF STEM image and EDS elemental maps at plane view of A) Zr-0.4Nb, B) Zr-0.5Nb, C) Zr-1.0Nb, and D) Zr-0.5Nb annealed at 1000 °C.

(not present in the unirradiated samples), whereas only spherical native precipitates were found in Zr-0.4Nb at 0.55 dpa. EDS maps in Fig. 2 A) and Fig. S6 A) shows that there are no observable differences in the microstructure and microchemistry after 0.55 dpa in Zr-0.4Nb. Most native precipitates in irradiated Zr-0.4Nb still contain both Fe and Nb, while only a few precipitates contain Nb alone. In Zr-0.5Nb at 1 dpa, there are numerous of native precipitates remaining in the matrix (see Fig. S6 B), similar to 0.55 dpa Zr-0.4Nb. However, a few platelets could be observed using high magnification STEM/EDS images as shown in Fig. 2 B).

For 0.55 dpa Zr-1.0Nb, the sample contains a high density of spherical native precipitates, as shown in Fig. 2C). Occasionally, large rod shaped Nb-rich precipitates (length greater than 200 nm) can be found in the matrix. On the other hand, at 1.0 dpa, a significant amount of platelets, containing only Nb, are observed under STEM mode throughout the sample (Fig. 2 D)). It is important to note that in order to image platelets under STEM mode, the sample does not need to be tilted to a specific orientation. All the STEM images presented in Fig. 2 were imaged in the orientation perpendicular to the beam direction and parallel to the irradiation surface.

Another major difference between Zr-1.0Nb at 1 dpa and the other alloys/conditions is the existence of partial dissolution of native precipitates, shown in Fig. 3. Indeed, Nb is not homogeneously distributed in the post-irradiated precipitates, which are depleted in Nb (and potentially Fe). Such dissolution phenomenon was not observed in 1.0 dpa Zr-0.5Nb. In addition, the EDS line scan measurement on this particular native particle shows only approximately 20 at.% Nb, though there might be a significant Zr matrix thickness effect. However, most non-dissolved native precipitates in the same sample showed a reduction of Nb content to approximately 60 at.% with a lamellae thickness below 50 μm, such that matrix effect are negligible. This reduced Nb content in the native precipitates is consistent reports of in-PWR neutron irradiated M5® alloy observations, (300−350 °C and fluence greater than $15 \times 10^{25}\ n/m^2$), which have reported 55 at.% Nb in the native precipitates [7].

More compositional details of platelets in 1.0 dpa Zr-1.0Nb are shown in Fig. 4 under higher magnification. The STEM BF image in Fig. 4 A) features a Nb-rich precipitate about 110 nm long and 25 nm wide. There is no higher Fe intensity inside the precipitate, which indicates no Fe enrichment in the precipitate. This is confirmed with EDS line scan over this particular precipitate in Fig. 4 B), which indicates only enrichment of Nb inside the precipitate. Fig. 4C) shows EDS line scan over a different precipitate, which shows no increase of Fe or Cr inside the precipitate but the enrichment of Nb. Based on the sample thickness, the Nb content in those platelets varies between 20 and 40 at.%. The Nb content in the neutron irradiation induced platelets (IIPs) has been reported to be as high as 60 at.% up to 2 PWRs irradiation cycles [14].

The size distribution of platelets is shown in Fig. S7. In total, more than 60 platelets were measured in 1 dpa Zr-1.0Nb. Most precipitates have a length between 50 and 120 nm and width less than 50 nm, with only a few having a length greater than 150 nm and a width greater than 50 nm. The sizes of platelets were measured based on STEM/EDS images taken parallel to irradiation surface, without tilting to specific zone axis for each grain. In this case, the variation of the grain orientations can affect the measured length and width of the precipitates.

The Zr-0.5Nb alloy annealed at 1000 °C and irradiated at 0.55dpa has a completely different microstructure than the other alloys. Similar to the observations in the unirradiated case, none of the spherical Nb-rich or Fe-rich precipitates could be observed. After irradiation, the matrix remains α-Zr phase. STEM/EDS images in Fig. 5 A) shows that the Nb segregated at the lath boundaries is now discontinuously distributed. Small portions of the lath boundaries also contain Fe. Decomposition of the Nb-rich β-Zr phase along the grain boundaries has been commonly observed in Zr-2.5Nb upon irradiation and heat treatment [27]. Therefore, thermal effects rather than irradiation are likely responsible for this phase separation. Thus, low temperature irradiation (350 °C) would cause a similar effect on Nb-rich lath boundaries in β-Zr quenched sample than decomposition of β-Zr phase in α+β field quenched Zr-2.5Nb sample at 500 °C for 10 h [27]. Higher magnification STEM/EDS image in Fig. 5 B) shows the presence of possible Nb-rich irradiation induced platelets away from the laths. They are isolated from the discontinuous lath boundaries and do not contain Fe, which is consistent with the observation of platelets in 1 dpa Zr-0.5Nb and 1 dpa Zr-1.0Nb.

3.3. HRSTEM characterization on 1.0dpa Zr-1.0Nb

Upon irradiation, precipitate/matrix interfaces act as sinks for point defects (PDs), which leads to irradiation induced segregation/

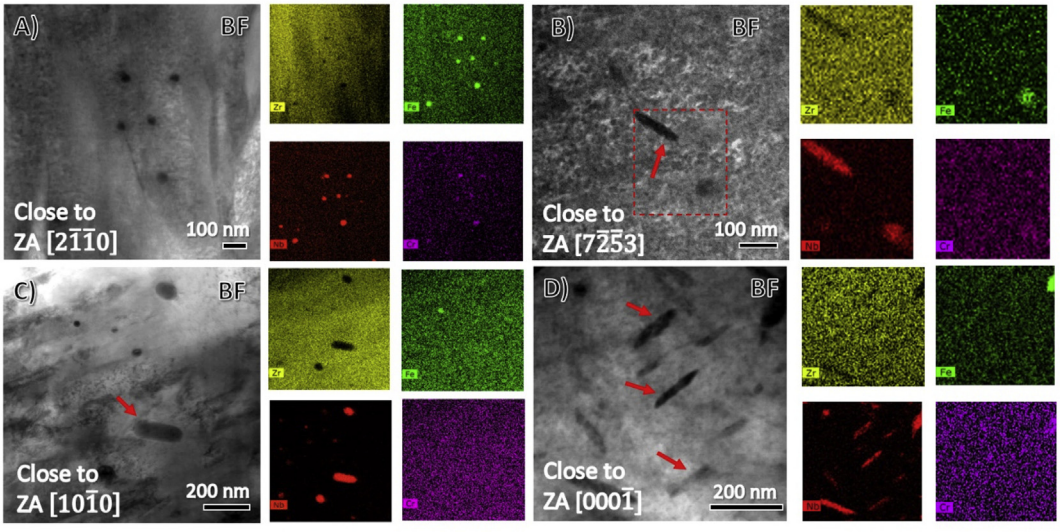

Fig. 2. BF STEM/EDS at plane view of A) 0.55 dpa Zr-0.4Nb, B) 1.0 dpa Zr-0.5Nb, C) 0.55 dpa Zr-1.0Nb, and D) 1.0 dpa Zr-1.0Nb.

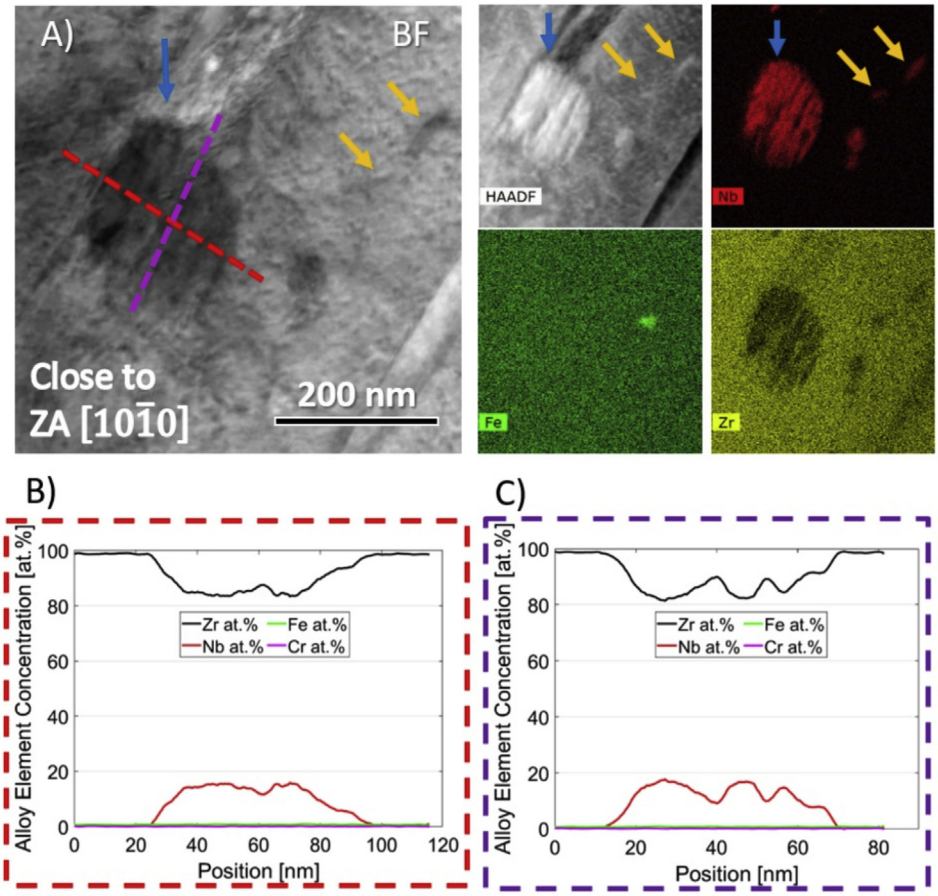

Fig. 3. A) STEM/EDS images show the dissolution of native precipitates, which is pointed by blue color arrows. Irradiation-induced platelets are pointed by orange color arrows. Dash lines presents the EDS line scan pathway. B) EDS line scan over native precipitate along red dash line. C) EDS line scan over native precipitate along purple dash line. (For interpretation of the references to color in this figure legend, the reader is referred to the Web version of this article.)

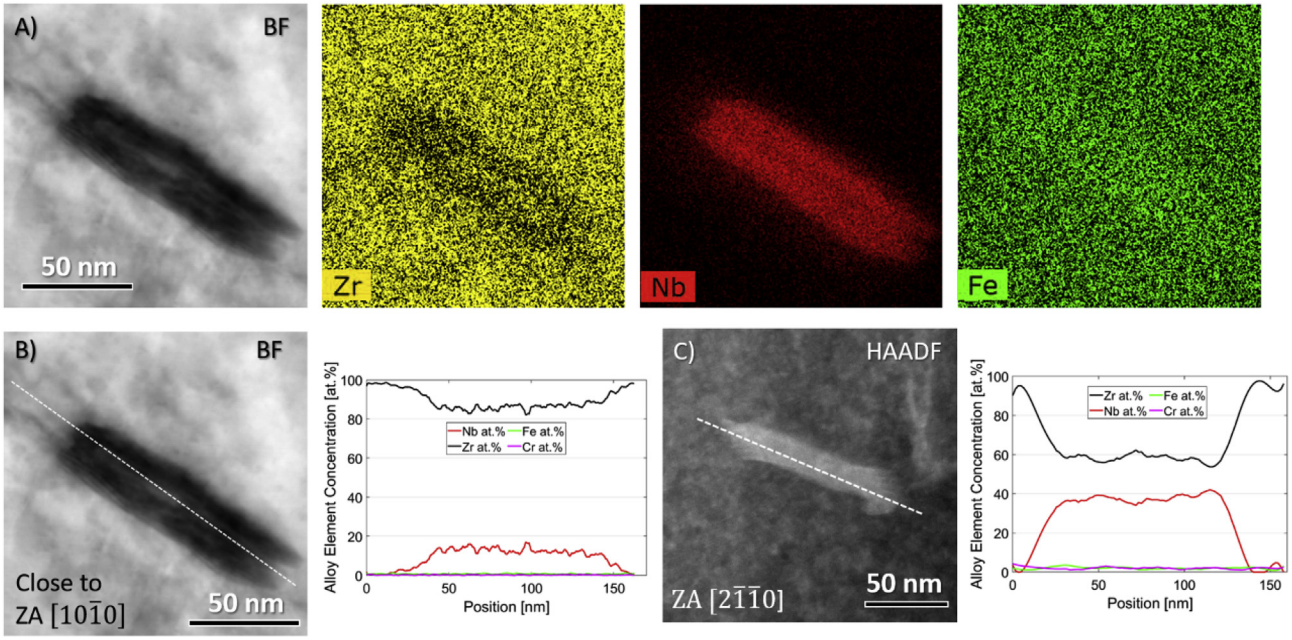

Fig. 4. A) High magnification STEM BF/EDS mapping of platelets. B)–C) EDS line scans over two platelets.

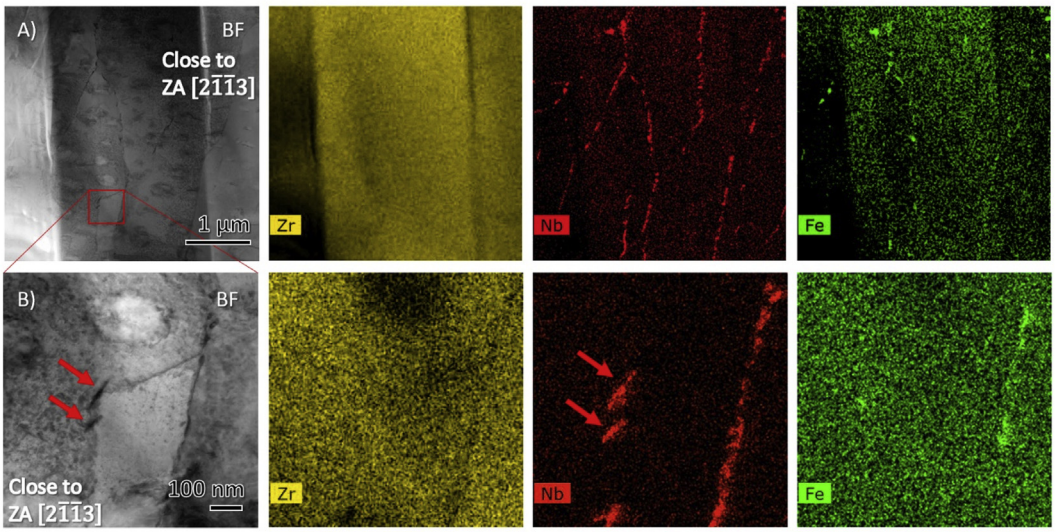

Fig. 5. STEM/EDS images at plane view of pre-annealed Zr-0.5Nb irradiated at 0.55dpa A) decomposition of Nb-rich laths boundaries, and B) possible irradiation induced precipitates in the Zr matrix away from the laths.

depletion though the inverse Kirkendall effect [16]. It is also well known that the coherency between the precipitates and surrounding matrix significantly affects the interface sink strengths [18]. Thus, since the interface sink strength may affect diffusion of alloying elements under irradiation, it is important to characterize the coherency and orientation relationship (OR) between the precipitate and matrix to understand the growth mechanism of platelets. Since HRSTEM is one of the available atomic-scaled characterization methods to obtain the OR between a precipitate and matrix, this method was performed on selected irradiated induced platelet.

Fig. 6 shows HAADF-STEM images of a typical platelet, which is about 100 nm in length and 20 nm in width. Higher magnification images inside the body of the platelet shows hexagonal lattice structure from [2$\bar{1}\bar{1}$0] zone-axis. The measured atomic spacing and the corresponding FFT further indicate that this platelet has a b.c.c crystal structure. In addition, the EDS results on the same platelet shows 40 at.% Nb in Fig. 4C). Since the Nb content in the model alloys is low, the maximum Nb solubility in β-Zr is 20 at.% based on available phase diagrams [19]. Thus, the irradiation induce platelet contains twice higher Nb content than the maximum Nb solubility in β-Zr. Furthermore, there is no enrichment of Fe inside the precipitate. Therefore, combining the HSRTEM/EDS experimental data and the results from literatures [4,7,28], this IIP has β-Nb crystal structure. In Fig. 6, the precipitate is at the $[1\bar{1}1]_{b.c.c.}$ zone axis. The FFT pattern of the matrix shows $[2\bar{1}\bar{1}0]_{h.c.p.}$ zone axis. The simulated diffraction patterns, shown in Fig. S8 by VESTA and JEMs, are consistent with the identified crystal structures. Therefore, the

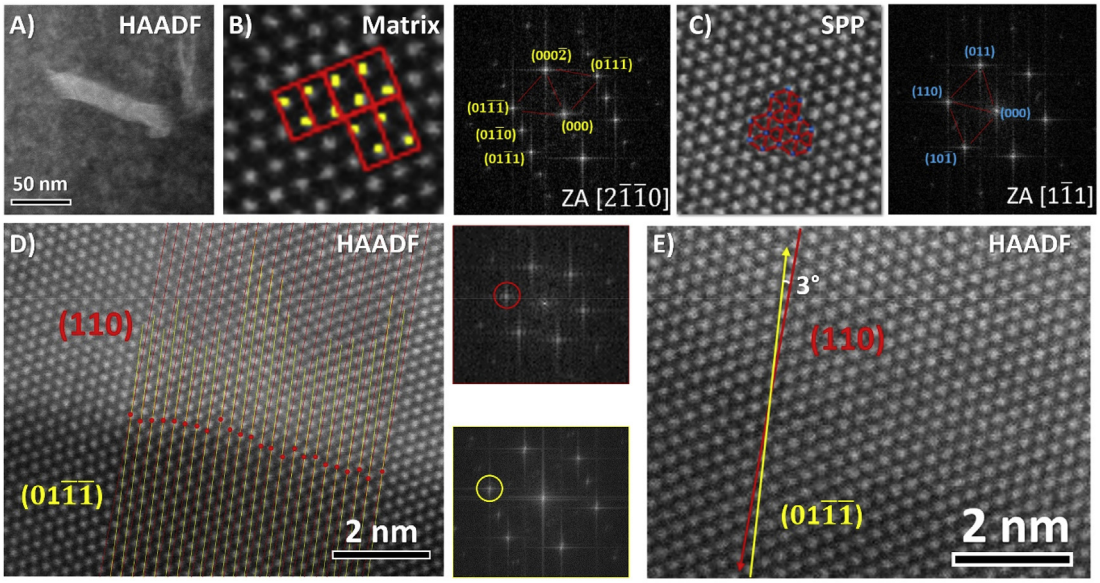

Fig. 6. A) STEM of a typical platelet in the matrix. B) and C) HRSTEM images taken from the inner part of the platelet and from Zr matrix. The inner body of the precipitate shows b.c.c Nb-rich platelet with a zone axis [1$\bar{1}$1] parallel to zone axis [2$\bar{1}\bar{1}$0] of h.c.p Zr matrix. D) HRSTEM of the interface between the body of platelets and matrix. The red points indicate the intersection of (01$\bar{1}\bar{1}$) and (110) planes. E) (110) platelets and (01$\bar{1}\bar{1}$) matrix plane have 2–3° rotation. (For interpretation of the references to color in this figure legend, the reader is referred to the Web version of this article.)

body of the precipitate at [$1\bar{1}1$] direction tend to align with [$2\bar{1}\bar{1}0$] direction of the matrix. The long axis of body is close to parallel to matrix $(01\bar{1}\bar{1})_{h.c.p}$ diffraction direction. Also, the (0002) plane of the matrix is parallel to (011) plane in the precipitate. This OR is the well-known Burgers OR between h.c.p. and b.c.c. structure [17,29], which is consistent with the OR reported between radiation induced precipitates and the matrix after the 10 MeV electron irradiation on Zr-2.5Nb (maximum dose level: 1.3 dpa; irradiation temperature; 440 °C) [3,14]. This OR was verified on other platelets, as shown in Fig. S9 and Fig. S10.

The interface between the platelet and matrix in Fig. 6 A) was magnified in Fig. 6D and E). Although the interface has a continuous transition between the two crystal structures, there is 2–3° rotation between the $(01\bar{1}\bar{1})$ and (110), which is consistent with the angle in the FFT patterns between these planes. The red dots in Fig. 6 D) are approximately the intersection of the planes, which might indicates the actual interfaces of h.c.p and b.c.c structures.

3.4. 4D-STEM characterization on 1.0 dpa Zr-1.0Nb

One of the imaging modes in 4D-STEM is nano-beam electron diffraction (NBED), where small convergence angle is used to generate nm-sized electron probe with separated diffraction disks. Previous works have demonstrated that NBED is capable of mapping strain with 0.1% precision across a μm field of view [30,31]. For coherent second phase precipitate (SPP) with different crystal structure than the matrix, lattices are distorted at the interface in order to maintain the coherency, which induce local strains [32]. In addition, strain energy plays a more important role than interfacial energy in determining the shape of coherent precipitates consisting of elements with differences in atomic radius [32]. Finally, upon irradiation, PDs are introduced into the material, which could induce additional strain in the Zr matrix affecting the precipitate growth [17]. Using NBED pattern acquired in 4D-STEM, it is possible to map strain at comparable precision as traditional geometric phase analysis in HRTEM over the whole precipitate and its surrounding matrix, make it a well-suited technique to understand the growth mechanism of platelets.

Zr-1.0Nb irradiated under 1 dpa dose was used for 4D-STEM measurement. HAADF image of the analyzed platelet and the FFT patterns of the platelet and matrix are shown in Fig. S10. The lattice structure is consistent with the OR described in Fig. 6. Diffraction disk positions were determined with sub-pixel precision following the method described in Ref. [30]. From all diffraction spots, two diffraction disks $\vec{g}_{i=1,2}$ corresponding to matrix $(000\bar{2})$/platelet (011) and matrix $(0\bar{1}1\bar{1})$/platelet $(\bar{1}01)$ were selected to generate strain maps (see SM section 3 for detailed strain calculation procedures). The resulting color-coded 2D d-spacing maps and strain maps are shown in Fig. 8. The strain maps include two uniaxial strain (ε_{xx} and ε_{yy}), shear strain (ε_{xy}), and rotation map (ε_{rot}). It is important to notice that the strain matrix is actually composed of lattice mismatch inherent to the h.c.p and b.c.c crystal structures and to actual strain in those lattices. Thus, the strain values resulting from this derivation are much larger than the true strain experienced by the two phases. A deconvolution of the two terms was not attempted in the 4D-STEM map as it is rather laborious to define the actual interface between the two phases.

A more detailed HRSTEM analysis of the two ends of the platelet is shown in Fig. 7C) and D), which indicates that the platelet is not fully coherent with visible edge dislocations at the interfaces. On the other hand, only one edge dislocation was observed nearby the platelet's long side.

Plane spacings of matrix $(000\bar{2})$/platelet (011) and matrix $(0\bar{1}1\bar{1})$/platelet $(\bar{1}01)$ are plotted in Fig. 8B) and C), respectively. The 4D-STEM measurements show that the Zr matrix contains multiple regions with d-spacing larger than 2.6 Å for both diffraction vectors. For the Nb-rich platelet, only the d-spacing for $\vec{g}_2$ is smaller than 2.5 Å, whereas the d-spacing for $\vec{g}_1$ is rather similar to the Zr matrix.

The strain maps in Fig. 8D) and E) shows a greater contrast between Zr matrix and platelets. For ε_{xx}, the platelet has compressive strain, with a lowest strain inside platelets, owes to lattice mismatch between the α-Zr and β-Nb. On the other hand, within the matrix itself, $(000\bar{2})$ planes are mostly strain-free, besides a couple of small regions. It is expected that local tensile strain in the Zr matrix basal direction correspond to a lattice expansion, potentially induced by non-resolvable point defects or small clusters/loops. For ε_{yy}, the two ends in the vicinity of platelet and matrix interface were under significant tensile strain. Despite the fact that no crystal defects were observed in the middle portion of the platelet from HRSTEM image, the platelet still remains under tensile strain. The observed high tensile strain will be discussed in more details in the next section. Multiple regions in the $(0\bar{1}1\bar{1})_{Zr}$ are also under tensile strain.

The rotation map presents the strain induced by plane rotation, where interfacial misfits generate nonzero values. Since any defects can cause crystal plane rotation [32], the strain fields in Fig. 8 G) and Fig. S12 best present the defect locations. A coupled of spots near the two ends of the platelets show localized high plane rotation induced strain fields, which corresponds to the identified edge dislocations in HRSTEM images.

4. Discussion

4.1. Precipitate density evolution as a function of dose and Nb content

The overall precipitate density results, calculated from STEM/EDS images and normalized by EELS thickness measurements, are summarized in Fig. S11. The most important observed trend is even if the irradiation induced platelets are lumped into the overall precipitate density, the precipitate density drops significantly for all alloys after irradiation. The overall precipitate density has reduced approximately by 30% for 0.55 dpa Zr-0.4Nb and 1 dpa Zr-0.5Nb compared to unirradiated samples, whereas the density of 1 dpa Zr-1.0Nb has decreased approximately by 50%. The reduction of density correlates to the atomic scale observation that the native precipitates are dissolving into the matrix upon irradiation (see Fig. 3). Comparing overall precipitate density of Zr-1.0Nb at 0.55 dpa and 1.0 dpa, there is a slightly increase of density, which is due to the precipitation of irradiation induced platelets. However, it is unclear if the overall precipitate density will be recovered at higher doses as more irradiation induced platelets nucleate and grow.

Precipitate density evolution of neutron irradiated M5® has been carefully studied in Ref. [7], using both TEM and synchrotron X-ray analysis. The native β-Nb precipitate density slightly increases from $1.1 \times 10^{20}\ m^{-3}$ to $1.2 \times 10^{20} m^{-3}$ at 4 dpa (1×10^{25} n/$m^2 = 2$ dpa [33]), and then continuously decreases to $0.6 \times 10^{20} m^{-3}$ at 16 dpa. On the other hand, the number density of platelets increases from 0 to about $1.5 \times 10^{22}\ m^{-3}$ at 4 dpa, and then remains relatively constant. Therefore, the overall precipitate density of neutron irradiated M5® increases by two magnitude compared to unirradiated sample, which is different from the precipitate density trends observed in proton irradiated Zr–Nb model alloys presented in this study.

This significant discrepancy on overall precipitate density between neutron and proton irradiated Zr–Nb alloys may be due to the different interaction of irradiation species with target materials. Due to competition between (i) disordering by atomic mixing and (ii) re-ordering by irradiation enhanced diffusion, precipitates can

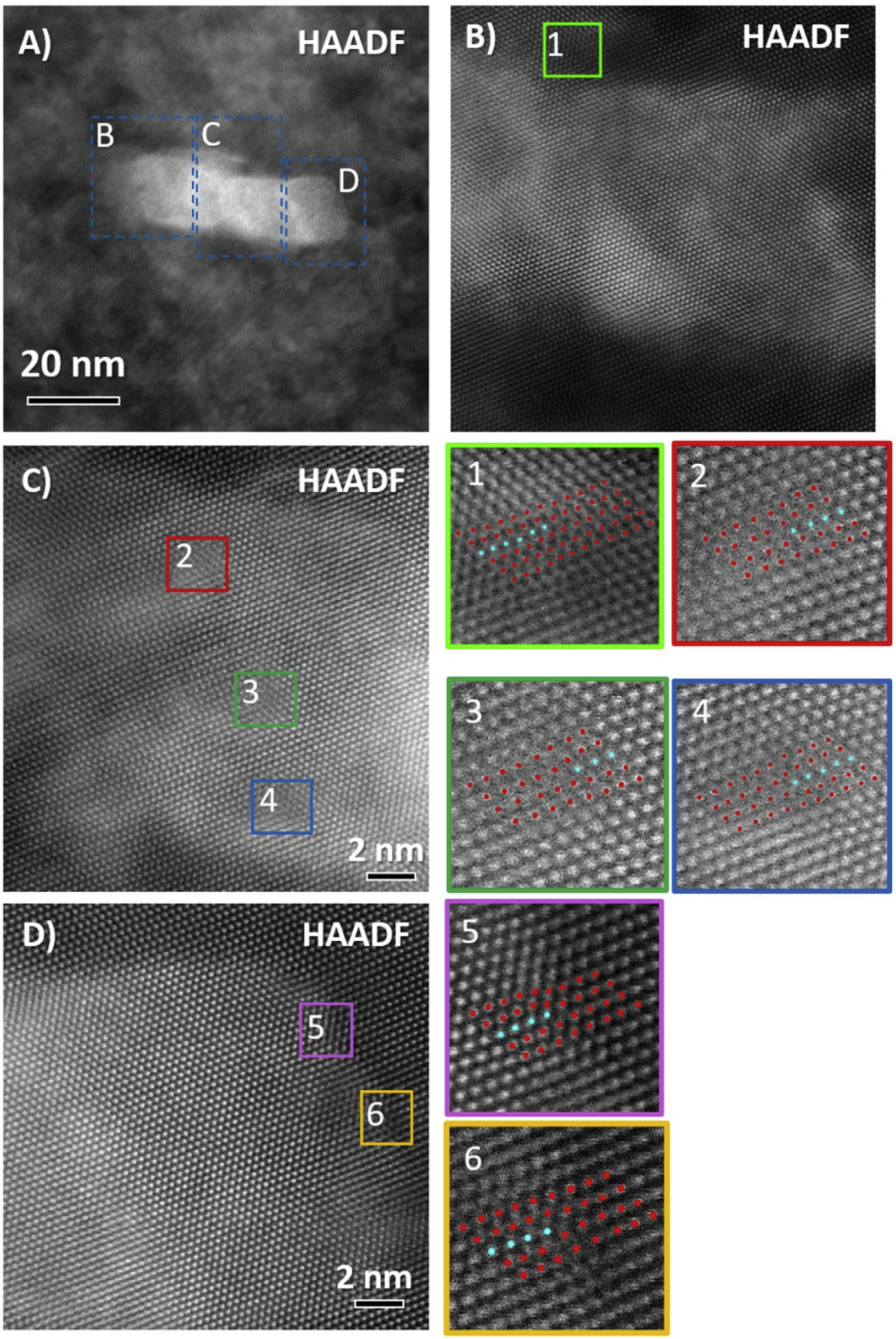

Fig. 7. HRSTEM images of A) entire irradiation induced platelet, B)-D) few defects (edge dislocations) found in the vicinity of the platelet/matrix interface. 1)-6) higher magnification of atomic scaled edge dislocation. The light blue dots represent the extra plane of atoms inside the platelet. (For interpretation of the references to color in this figure legend, the reader is referred to the Web version of this article.)

stabilize to a steady state size. This process is the so-called "patterning" phenomenon [34]. However, patterning requires atomic relocation distances greater than nearest neighbor distances. Since proton irradiation does not generate energetic cascades or long relocation distance, patterning does not happen upon proton irradiation. On the other hand, neutron irradiation, with deep penetration depth, produces energetic cascades and results in patterning in irradiated materials. In that sense, instead of growing high density platelets, the platelets induced by proton irradiation keep growing larger. Therefore, the overall precipitate density is reduced upon proton irradiation, but the size of formed platelets is larger than that of neutron irradiation induced platelets. On the other hand, studies in Refs. [4,34] have also claimed that 3.6 MeV proton irradiation induces similar microstructure, in terms of precipitation of irradiation induced platelets, in Zr-2.5Nb at 720 K and 0.94 dpa compared to in-reactor neutron irradiation. The size difference between neutron and proton irradiation induced platelets has been attributed to irradiation time (i.e. diffusion) instead of total dose level. Unfortunately, although the stability of native precipitate upon proton irradiation has been investigated in the

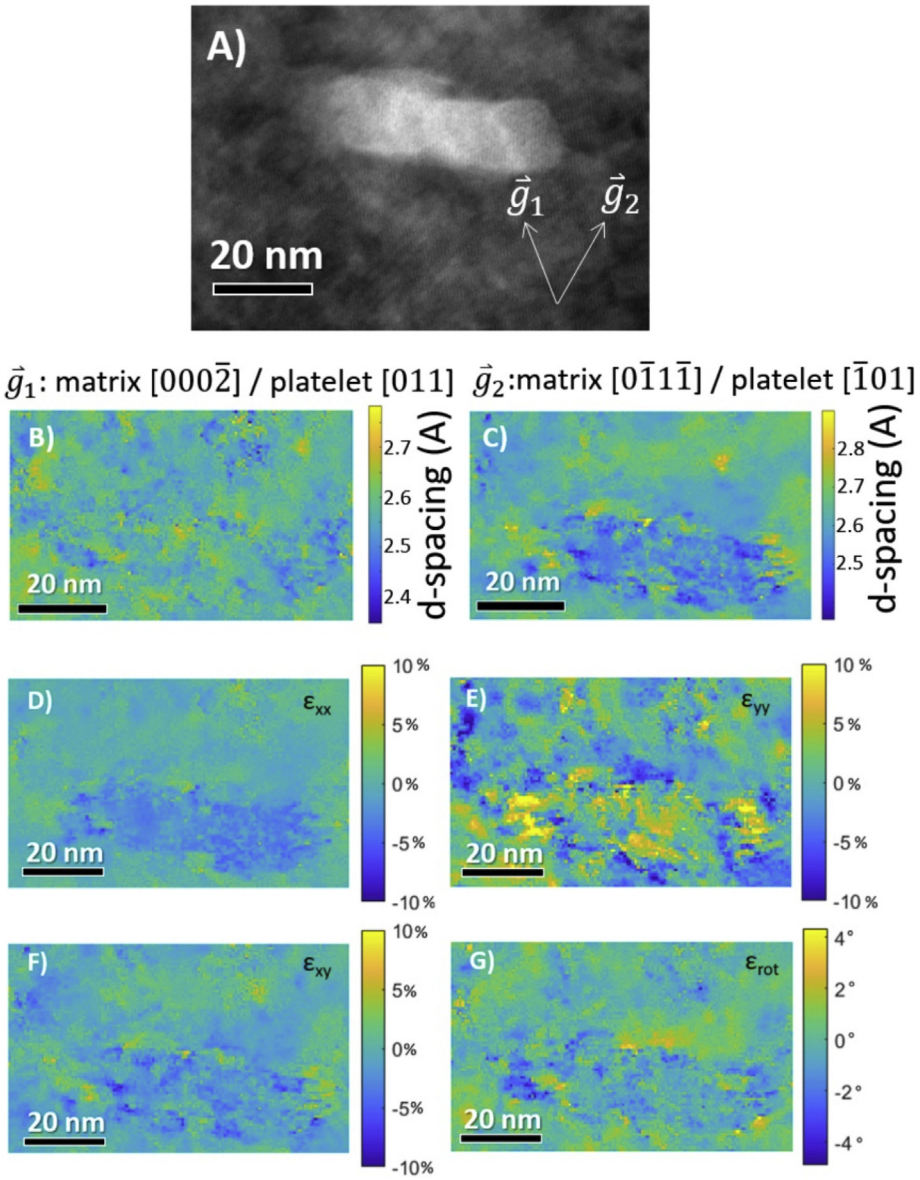

Fig. 8. 4D-STEM analysis of platelets in Zr matrix. A) HAADF-STEM image of irradiation induced platelet, studied for strain map. B) and C) d-spacing maps along $\vec{g}_1$ and $\vec{g}_2$ diffraction direction. D) to G) Strain maps containing the uniaxial strain (ε_{xx} *and* ε_{yy}), shear strain (ε_{xy}), and rotation (ε_{rot}) maps.

literature [4], there is no precipitate density and size distribution reported for proton irradiated Zr–Nb alloys.

4.2. Defect and strain field in the vicinity of irradiation induced platelets

From the HRSTEM images, the two ends of the platelets have semicoherent interfaces, whereas the platelet's length interfaces are coherent with the matrix. This finding is different to the HRSTEM analysis of the neutron irradiated M5® in Ref. [14], which reported incoherent rather than semicoherent interface, at the ends of the platelet. However, the neutron irradiation-induced platelets were analyzed along the [0001] matrix zone axis, whereas the proton irradiation-induced platelets in this study was analyzed at the [2$\bar{1}\bar{1}$0] matrix zone axis. Therefore, from a different zone axis, the atomic arrangement at the interface might appear different, potentially affecting the imaging of dislocations.

For semicoherent interface, the spacing D between edge dislocations can be calculated using equations (1) [32]:

$$D = \frac{d^{Zr}_{(000\bar{2})} \times d^{Nb}_{(011)}}{d^{Zr}_{(000\bar{2})} - d^{Nb}_{(011)}}$$

D_m is the D measured from the $d^{Zr}_{(000\bar{2})}$ and $d^{Nb}_{(011)}$ values from the HRSTEM images, and is measured to be 3.93 nm. The actual spacing between edge dislocations at the platelet's end, from Fig. 7 D), is 3.83 nm, which is only 2.8% less than theoretical calculation. If spacing D is calculated using $d^{Zr}_{(000\bar{2})}$ and $d^{Nb}_{(011)}$ based on relaxed crystal structure [7,14], then D_r is equal to 2.49 nm, which is 35% less than the measured spacing between edge dislocations. Since D_m is greater than D_r, the dislocations did not fully relieve the coherency strains, such that there should be a long-range residual strain field nearby the two ends of the platelets [32].

As shown in Figs. 6 and 7C), the $(01\bar{1}\bar{1})_{Zr}$ and $(110)_{Nb}$ diffraction

direction are almost perpendicular to the platelet's length interface/long body axis, and only 2–3° from being parallel to each other. The d-spacing mismatch between $d^{Zr}_{(01\bar{1}\bar{1})}$ and $d^{Nb}_{(110)}$, based on relaxed crystal structure, is 5.2%. However, based on HRSTEM images measurement, d-spacing mismatch between these two planes is only 1.45%. Both calculations show that the mismatch is relatively small. Thus, it is theoretically possible to obtain a coherent interface at the platelet's lengths. Since the Nb lattice planes tend to match with the Zr lattice planes, this causes local plane rotation to keep the interface coherent, which could explain the relatively high ε_{rot} observed in the two highlighted regions in Fig. S12. Thus, the ε_{rot} map shows the residual coherent strain field at the platelet's length interfaces, as well as edge dislocation induced strain fields nearby the platelet's ends.

Since [14] has reported that the neutron irradiation induced platelets are laying on the basal plane, it is most likely that the HAADF image in Fig. 8 A) is the cross section of the proton irradiation induced platelets. Therefore, the short axis direction should be the thickness direction of the platelet. Thus, the entire thickness area should be semicoherent with the Zr matrix. Since semi-coherent interface should still contain residual coherent strain, the high ε_{yy} region measured in the middle portion of the platelet, in Fig. 8 E), could be explained by the coherent strain. Indeed, there is an overlapping of the semi-coherent interfaces in the field of view when acquiring HRSTEM image and 4-D STEM scan.

4.3. OR comparison of proton and neutron IIPs

In this study, we have reported the OR of platelet and matrix is $[2\bar{1}\bar{1}0]_{h.c.p}$ // $[1\bar{1}1]_{b.c.c}$ and $(0002)_{h.c.p}//(011)_{b.c.c}$, which is consistent with Burgers OR reported in 1.2 dpa Zr-2.5Nb [3]. For neutron irradiated M5®, the reported OR in M5® is $[1\bar{2}10]_{h.c.p}$ // $[100]_{b.c.c}$ and $(0001)_{h.c.p}//(011)_{b.c.c}$ [14]. The apparently different OR is due to characterization at different zone. Since one of the purposes to perform proton irradiation on Zr–Nb alloy is to emulate neutron irradiation effect, it is important to compare the OR of the proton IIPs with neutron IIPs at the same Zr matrix zone. Based on the OR identified for both proton irradiation induced platelet and neutron irradiation induced platelet, we constructed a 3D model of the h.c.p and cubic unit cell, and tilted to $[0001]_{h.c.p.}$ zone pointed out of the view plane, which is shown as top view in Fig. 9. For both proton and neutron IIPs, $[011]_{b.c.c.}$ points out of plane. It is concluded that the following $\{11\bar{2}0\}_{h.c.p}//\{100\}_{b.c.c}$, $\{0001\}_{h.c.p}//\{011\}_{b.c.c}$ and $\{10\bar{1}0\}_{h.c.p}//\{01\bar{1}\}_{b.c.c}$. represent the OR of variant planes between h.c.p Zr and b.c.c Nb.

To confirm that we indeed have the expected OR at $[0001]_{h.c.p.}$, another TEM lamella was fabricated for HRSTEM experiment. As shown in Fig. 10, HRSTEM image of an IIP has been taken at $[0001]_{h.c.p.}$ zone. The Zr atoms are arranged in hexagonal rings, which are the typical $[0001]_{h.c.p}$ zone structure. Nb atoms are in cubic arrangement and correspond to [011]. In addition, $(200)_{b.c.c}$ is

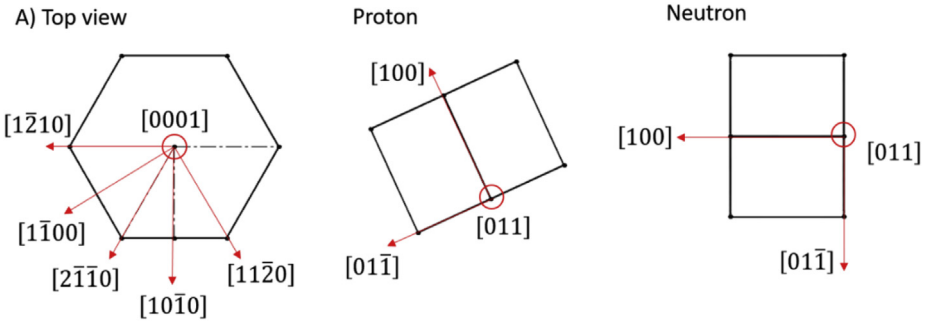

Fig. 9. Top view of 3D modelled OR between h.c.p. Zr and b.c.c. Nb unit cells.

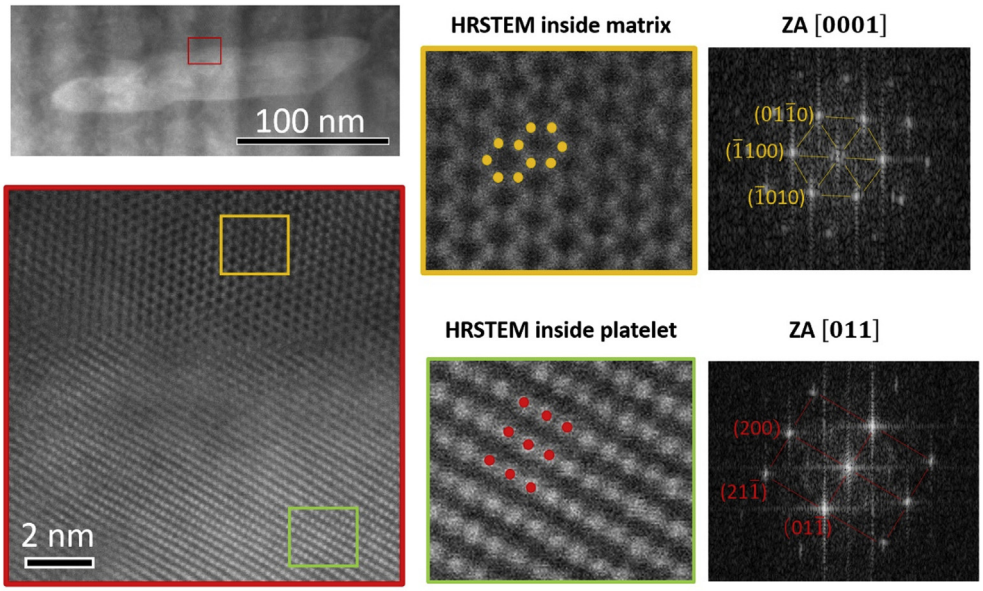

Fig. 10. HAADF HRSTEM and FFT investigation of OR between platelet and matrix at $[0001]_{h.c.p.}$ zone.

parallel with $(\bar{1}2\bar{1}0)_{h.c.p.}$. Thus, OR is $[\bar{1}2\bar{1}0]_{h.c.p}$ // $[200]_{b.c.c}$ and $(0001)_{h.c.p}//(011)_{b.c.c}$. This exactly matches with OR indexed in Ref. [14] on neutron irradiated materials. Thus, the irradiation induced β-Nb platelet can align their b.c.c crystal structure to the h.c.p Zr based on the identified variant planes above, such as $(01\bar{1})_{b.c.c}$//three $\{10\bar{1}0\}_{h.c.p}$ variant planes. Therefore, platelets could eventually grow along different preferential directions which are identical to one another.

4.4. Growth mechanism of platelets

The evolution of precipitates is strongly affected by irradiation through three major mechanisms: (i) radiation mixing, (ii) radiation-enhanced diffusion, and (iii) radiation-induced segregation (RIS) [16,18]. For radiation mixing, atoms are redistributed in the collision cascades, which causes the atoms in precipitates to be ballistically driven back into the matrix, usually resulting in precipitate dissolution [16]. On the other hand, irradiation introduces more PDs into the matrix. The diffusion coefficient under irradiation, increases as the result of the increased PDs concentration [18]. The irradiation-enhanced diffusion usually competes with atomic mixing to reach an equilibrium growth rate of the precipitate. Indeed, as the matrix becomes supersaturated because of radiation mixing, radiation enhanced diffusion drives the system back to equilibrium. Lastly, radiation induces segregation of solute atoms to the sinks through inverse Kirkendall effect [17], such that solute atoms with small flux against the vacancy flux, or bounded to interstitials, would be enriched at the sinks. Then, if the local solute concentration becomes larger than the solubility limit, precipitation and subsequent growth of particle would occur. There is a strong effect of solute size on the particle growth by RIS. In general, undersized solute atoms preferentially exchange with solvent atoms in interstitial sites and migrate as interstitials towards the precipitate sink, whereas oversized solute atoms migrate against the vacancy flux, away from the precipitate sink [18]. Thus, any size difference would results in enrichment of undersized solute and a depletion of oversized solute near defect sinks.

In the light of these well-known irradiation effects, three main growth mechanisms of Nb-rich precipitates can be drawn based on the thermodynamic equilibrium of the unirradiated material.

a. The Nb in Zr–Nb alloys is not at equilibrium in the unirradiated material: It is well-known that Nb is a sluggish diffusing species in ZrNb alloys [6,17]. In addition, the Nb solubility limit in ZrNb alloys is not well defined, such that the Nb maybe oversaturated in the matrix in the unirradiated state. Study in Ref. [6] has reported as low as 0.07 at.% of Nb in Zr matrix of low-Tin ZILO, whereas Zr–Nb binary model alloys contain 0.2–0.4 at.% [5,6]. Under that hypothesis, radiation would create nucleation sites for Nb-rich precipitates and these precipitates would grow under irradiation via radiation enhanced diffusion. This mechanism is supported by the fact that the precipitates formed under irradiation are actually stable under subsequent thermal annealing [2].
b. Native precipitate dissolution induces precipitation of Nb-rich platelets: The native precipitates (β-Nb and Laves phases) are mostly spherical and their interface with the matrix is most likely incoherent [14]. As reported in Ref. [16], incoherent β-Nb precipitates are not stable under irradiation and tends to dissolve back into the matrix. Indeed, the particle density in both proton irradiated Zr–Nb model alloys (see Fig. S11) and neutron irradiated M5® [7] shows reduction of native precipitates after irradiation. Consequently, solute Nb content increases and would be balanced by precipitation of coherent Nb-rich particles to reach steady-state Nb concentration in the matrix [18].
c. Nb-rich platelets grow via RIS: An interfacial dislocation acts as a sink, potentially biased towards interstitials, that strongly attracts PDs and could result growth of irradiation induced precipitates through inverse Kirkendall effect [18].

The coherency of the precipitate with the matrix can also affect the growth mechanism. Incoherent precipitates can be considered strong, biased or unbiased, PDs [18]. On the other hand, coherent precipitate does not contain as much defective segment to absorb PDs. Precipitates are thus considered a variable bias sink [18]. Consequently, the coherency strain field also affects the diffusion of PDs to the interface since the source of the attraction of PDs to the sink is the relief of the strain field [18].

From the 4D-STEM strain mapping in the vicinity of the irradiation induced platelets, it is proposed that the growth of the platelets is driven by the local strain field and accelerated by irradiation. Without irradiation, Nb is considered a slow substitutional diffuser [6,17]. Considering the smaller size of the Nb compared to Zr (about 8%), Nb would be relatively more concentrated as the interstitial PDs induced by irradiations. From the 4D-STEM characterization, the matrix is always under tensile strain, which indicates lattice expansion along both $(000\bar{2})$ and $(0\bar{1}1\bar{1})$ plane directions. A positively strained matrix lattice would also lower the migration barrier for interstitial Nb in Zr–Nb alloys. This effect would be especially prominent under irradiation. A relatively higher concentration of Nb interstitials would tend to migrate faster to the SPP. Considering, the areas nearby both ends of the platelet, which are under higher relative tensile strain along the matrix $(000\bar{2})$ and $(0\bar{1}1\bar{1})$, the most of the Nb PDs interstitials would diffuse at the platelets' ends to relieve the tensile coherency strain.

In addition, the edge dislocation near the semicoherent interface at the ends of the SPP can act as bias sinks for Nb PDs interstitials [18]. Consequently, Nb interstitial atoms would diffuse up the tensile stress gradient generated by dislocations and coherency strain fields to the ends of the SPP and, as a result would enhance the platelet growth. It is also worth noting that not only interstitial flux can be relatively enriched in Nb but the vacancy flux as well via vacancy drag effect [35]. Vacancy-solute drag occurs when the solute and the vacancy diffuse as a complex because of attractive binding energy and low migration barriers. The attractive binding energy and positive drag ratio of Ni, Fe, and Cr in α-Zr calculated in Ref. [35] could explain the strong correlation between solute-rich nanoclusters near vacancy type dislocation loops in Zr alloys [36,37]. The diffusion of Nb in α-Zr has been modelled in Ref. [38], showing an attractive vacancy-Nb solute binding energy. Therefore, it is also possible that vacancies diffuse with Nb as a complex to the dislocation sink, which would result in the growth of irradiation induced platelets. In summary, under the influence of coherency strain and irradiation, once the platelets form, they act as sinks to attract more Nb atoms to diffuse to their semicoherent interfaces for further growth.

5. Conclusions

Zr–Nb model alloys have been proton irradiated up to 1 dpa at 350 °C. The irradiation induced microstructure and microchemistry have been characterized using TEM/STEM/EDS/HRSTEM. Important conclusions from this study are as follows:

- Proton irradiation induces the formation of β-Nb platelets approximately 20–100 nm in length, containing 10–40 at.% Nb in Zr-0.5Nb and Zr-1.0Nb irradiated at 1.0 dpa. There are no

significant irradiation induced precipitation in any of the samples irradiated at 0.55 dpa.

- Particle densities measured by STEM/EDS show a reduction of total particle density after proton irradiation, implying that incoherent native SPPs have dissolved in the matrix. This dissolution of native precipitates is verified by STEM/EDS analysis.
- Although neutron irradiation induces smaller but denser Nb-rich precipitates compared to proton irradiation, likely because of greater atomic relocation distances, proton irradiation is certainly a good process to mimic neutron irradiation effect on Zr–Nb alloys, pending a parametric study to optimized the proton irradiation conditions.
- HRSTEM analysis show that irradiation induced precipitates have a Burgers ORs ($[1\bar{1}1]//[2\bar{1}\bar{1}0]$ and $(0002)//(011)$) with the matrix, which is similar to the identified ORs of irradiation induced precipitates in neutron irradiated M5® [15]. The interface of the platelet's two ends are semicoherent while the top/bottom interface are mostly coherent. Theoretical dislocation spacing calculations indicate that a relatively significant coherency strain field still exist at the platelet's ends albeit the presence of dislocations.
- Strain maps around irradiation induced Nb-rich platelets have been measured for the first time, using 4D-STEM. Areas with positive strain in the ε_{yy} map indicate platelet has high tensile strain along the thickness direction. The ε_{rot} map clearly show the residual coherent strain field at the platelet's length interfaces, and the dislocation induced strain fields nearby the platelet's two ends.
- The growth mechanism of the platelets is mainly driven by the strain field induced by interface coherency and dislocation. Since the strain fields are larger at the platelet's ends, this represents the preferential growth direction of irradiation induced precipitate. Indeed, irradiation both enhances the diffusion and induces segregation of Nb (via PDs interstitial binding and/or solute vacancy drag) to the ends of the platelets.

Data availably

The raw/processed data required to reproduce these findings cannot be shared at this time as the data also forms part of an ongoing study.

Acknowledgements

This work has been performed within the framework of the international MUZIC (Mechanistic Understanding of Zirconium Corrosion) program. The authors gratefully acknowledge the industrial support from EDF, EPRI, Naval Nuclear Laboratory, Rolls-Royce, Westinghouse and Wood. This work has been awarded through a Rapid Turnaround Experiment under DOE Idaho Operations Office Contract DEAC07-051D14517 as part of a Nuclear Science User Facilities Experiments. Support of NRC Faculty Development program is also acknowledged. The author would like to thank Dr. Yaqiao Wu, Joanna Taylor, and Jatuporn Burns for the aid to accomplish the characterization experiment at the Center of Advanced Energy Studies, thank Prof. Kumar Sridharan, Dr. Li He and Kim Kriewaldt at University of Wisconsin Ion Beam Laboratory for the successful proton irradiation experiments as well as thank the entire MUZIC community for insightful discussions and guidance over the years. High-resolution STEM and 4D STEM characterization by C. Z. and P. M. V. was supported by the Department of Energy Basic Energy Sciences (DE-FG02-08ER46547). Facilities for materials characterization including electron microscopy at UW-Madison are supported by the Wisconsin MRSEC (DMR-1720415).

Appendix A. Supplementary data

Supplementary data to this article can be found online at https://doi.org/10.1016/j.actamat.2019.08.012.

References

[1] C. Lemaignan, Physical phenomena concerning corrosion under irradiation of Zr alloys, in: Zirconium in the Nuclear Industry: 13th International Symposium, ASTM STP 1423, 2001, pp. 20–29.
[2] C. Coleman, R. Gilbert, G. Carpenter, G. Weatherly, Precipitation in Zr–2.5 Wt.-% Nb during neutron irradiation, in: Phase Stability during Irradiation; Pittsburgh; Pa.; 5-9 Oct. 1980, 1980, pp. 587–599.
[3] O.T. Woo, G.M. McDougall, R.M. Hutcheon, V.F. Urbanic, M. Griffiths, C.E. Coleman, Corrosion of Electron- Irradiated Zr-2.5Nb and Zircaloy-2, 2000, pp. 709–734.
[4] C.D. Cann, C.B. So, R.C. Styles, C.E. Coleman, Precipitation in Zr- 2.5Nb enhanced by proton irradiation, J. Nucl. Mater. 205 (C) (1993) 267–272.
[5] Z. Yu, A. Couet, M. Bachhav, Irradiation-induced Nb redistribution of ZrNb alloy: an APT study, J. Nucl. Mater. 516 (1 April 2019) 100–110.
[6] E. Francis, R.P. Babu, A. Harte, T.L. Martin, P. Frankel, D. Jädernäs, J. Romero, L. Hallstadius, P.A.J. Bagot, M.P. Moody, M. Preuss, Effect of Nb and Fe on damage evolution in a Zr-alloy during proton and neutron irradiation, Acta Mater. (2018).
[7] S. Doriot, B. Verhaeghe, J.L. Béchade, D. Menut, D. Gilbon, J.P. Mardon, J.M. Cloué, A. Miquet, L. Legras, Microstructural Evolution of M5™ Alloy Irradiated in PWRs up to High Fluences - Comparison with Other Zr- Based Alloys, ASTM Special Technical Publication, 2015, pp. 759–799.
[8] R. Verlet, Influence of Irradiation and Radiolysis on the Corrosion Rate and Mechanisms of Zirconium Alloys, 2015.
[9] Y. Matsukawa, H.L. Yang, K. Saito, Y. Murakami, T. Maruyama, T. Iwai, K. Murakami, Y. Shinohara, T. Kido, T. Toyama, Z. Zhao, Y.F. Li, S. Kano, Y. Satoh, Y. Nagai, H. Abe, The effect of crystallographic mismatch on the obstacle strength of second phase precipitate particles in dispersion strengthening: bcc Nb particles and nanometric Nb clusters embedded in hcp Zr, Acta Mater. 102 (C) (2016) 323–332.
[10] V. Urbanic, J. Lesurf, A. Johnson, Effect of aging and irradiation on the corrosion of Zr-2.5 wt, per cent Nb, Corrosion 31 (1) (1975) 15–20.
[11] A. Couet, A.T. Motta, A. Ambard, The coupled current charge compensation model for zirconium alloy fuel cladding oxidation: I. Parabolic oxidation of zirconium alloys, Corros. Sci. 100 (2015) 73–84.
[12] C. Toffolon-Masclet, P. Barberis, J.C. Brachet, J.P. Mardon, L. Legras, Study of Nb and Fe precipitation in α- phase temperature range (400 to 550°C) in Zr- Nb-(Fe- Sn) alloys, J. ASTM Int. (JAI) 2 (5) (2005) 1–18.
[13] P. Barberis, D. Charquet, V. Rebeyrolle, Ternary Zr– Nb–Fe(O) system: phase diagram at 853 K and corrosion behaviour in the domain Nb < 0.8%, J. Nucl. Mater. 326 (2) (2004) 163–174.
[14] J. Ribis, S. Doriot, F. Onimus, Shape, orientation relationships and interface structure of beta- Nb nano- particles in neutron irradiated zirconium alloy, J. Nucl. Mater. 511 (2018) 18–29.
[15] K. Nuttall, D. Faulkner, The effect of irradiation on the stability of precipitates in Zr-2.5 WT% Nb alloys, J. Nucl. Mater. 67 (1) (1977) 131–139.
[16] A.A. Turkin, A.V. Buts, A.S. Bakai, Construction of radiation- modified phase diagrams under cascade-producing irradiation: application to Zr–Nb alloy, J. Nucl. Mater. 305 (2) (2002) 134–152.
[17] A.T. Motta, D.R. Olander, Light Water Reactor Materials, American Nuclear Society, La Grange Park, Illinois, 2017-2017.
[18] G.S. Was, Fundamentals of Radiation Materials Science: Metals and Alloys, Berlin, Heidelberg: Springer Berlin Heidelberg, Berlin, Heidelberg, 2007.
[19] J. Abriata, J. Bolcich, The Nb–Zr (Niobium–Zirconium) system, Bulletin of Alloy Phase Diagrams 3 (1) (1982) 34–44.
[20] A. Couet, A.T. Motta, R.J. Comstock, Hydrogen pickup measurements in zirconium alloys: relation to oxidation kinetics, J. Nucl. Mater. 451 (1–3) (2014) 1–13.
[21] J. Romero, J. Partezana, R.J. Comstock, L. Hallstadius, A.T. Motta, A. Couet, Evolution of hydrogen pickup fraction with oxidation rate on zirconium alloys, in: Top Fuel Reactor Fuel Performance, Zurich, Switzerland, 2015, pp. 476–482.
[22] R.E. Stoller, M. Toloczko, S. Dwaraknath, On the use of SRIM/TRIM for computing radiation damage exposure, Nucl. Instrum. Methods Phys. Res. Sect. B Beam Interact. Mater. Atoms 310 (2013).
[23] R.F. Egerton, Electron Energy- Loss Spectroscopy in the Electron Microscope, 3 ed., Boston, MA: Springer US, Boston, MA, 2011.
[24] A. Harte, M. Griffiths, M. Preuss, The characterisation of second phases in the Zr-Nb and Zr-Nb-Sn-Fe alloys: a critical review, J. Nucl. Mater. 505 (2018) 227–239.
[25] Y.H. Jeong, H.G. Kim, D.J. Kim, B.K. Choi, J.H. Kim, Influence of Nb concentration in the α- matrix on the corrosion behavior of Zr– xNb binary alloys, J. Nucl. Mater. 323 (1) (2003) 72–80.

[26] D. Srivastava, P. Mukhopadhyay, S. Banerjee, S. Ranganathan, Morphology and substructure of lath martensites in dilute Zr-Nb alloys, Mater. Sci. Eng. A 288 (1) (2000) 101–110.
[27] V.F. Urbanic, R.W. Gilbert, Effect of Microstructure on the Corrosion of Zr-2.5Nb Alloy, High-Temperature Oxidation and Sulphidation Processes, 1990. Hamilton, Ontario, Canada.
[28] R. Verlet, in: E. Saint-Etienne, K. Wolski (Eds.), Influence de l'irradiation et de la radiolyse sur la vitesse et les mécanismes de corrosion des alliages de zirconium; Influence of irradiation and radiolysis on the corrosion rate and mechanisms of zirconium alloys, 2015.
[29] H.S. Sen, T. Polcar, Vacancy-interface-helium interaction in Zr-Nb multi-layer system: a first-principles study, J. Nucl. Mater. (2019).
[30] V.B. Ozdol, C. Gammer, X.G. Jin, P. Ercius, C. Ophus, J. Ciston, A.M. Minor, Strain mapping at nanometer resolution using advanced nano- beam electron diffraction, Appl. Phys. Lett. 106 (25) (2015).
[31] T.C. Pekin, C. Gammer, J. Ciston, A.M. Minor, C. Ophus, Optimizing disk registration algorithms for nanobeam electron diffraction strain mapping, Ultramicroscopy 176 (C) (2017) 170–176.
[32] D.A. Porter, K.E. Easterling, M. Sherif, Phase Transformations in Metals and Alloys, third ed., 3 ed, 2009 (Revised Reprint), pg 149-163.
[33] C. Lemaignan, A.T. Motta, Zirconium Alloys in Nuclear Applications, B. R. T. Frost, 1994.
[34] G. Was, Challenges to the use of ion irradiation for emulating reactor irradiation, J. Mater. Res. 30 (9) (2015) 1158–1182.
[35] P.A. Burr, M.R. Wenman, B. Gault, M.P. Moody, M. Ivermark, M.J.D. Rushton, M. Preuss, L. Edwards, R.W. Grimes, From solid solution to cluster formation of Fe and Cr in α- Zr, J. Nucl. Mater. 467 (Part 1) (2015) 320–331.
[36] A. Harte, D. Jädernäs, M. Topping, P. Frankel, C.P. Race, J. Romero, L. Hallstadius, E.C. Darby, M. Preuss, The effect of matrix chemistry on dislocation evolution in an irradiated Zr alloy, Acta Mater. 130 (2017) 69–82.
[37] G. Sundell, M. Thuvander, P. Tejland, M. Dahlbäck, L. Hallstadius, H.O. Andrén, Redistribution of alloying elements in Zircaloy-2 after in-reactor exposure, J. Nucl. Mater. 454 (1–3) (2014) 178–185.
[38] V.P. Ramunni, A.M.F. Rivas, Diffusion calculations with two atomic models in h.c.p Zr-Nb diluted alloys, Mater. Chem. Phys. 197 (2017) 163–180.